CrossMark

Evolution of mesoporous TiO$_2$ during fast sol–gel synthesis

Rong Fu[1] · Qianqian Yin[1] · Xiaoling Guo[2] ·
Xing Tong[2] · Xiangdong Wang[1]

Abstract Mesoporous TiO$_2$ nanoparticles were synthesized by a fast sol–gel method using polyethylene glycol (PEG) and polyacrylamide as bi-template followed by two-step calcination under nitrogen and air atmosphere. The effects of factors such as the solvent volume, amount of water, medium pH, and amount and molecular weight of PEG on the sol–gel reaction rate were studied based on analysis of zeta potential measurements. The results showed that lower ethanol volume, lower pH, greater water volume, and higher PEG molecular weight led to faster sol–gel reaction rate with shorter gelation time, with pH and water volume being the most influential amongst these factors. The evolution during the fast sol–gel process was also investigated based on the infrared (IR) spectrum. The results indicated that the fast sol–gel process occurred due to intermolecular hydrogen bonding between hydrolysates of Ti alkoxides and the bi-template. The samples were characterized by X-ray diffraction (XRD) analysis, transmission electron microscopy (TEM), and N$_2$ adsorption–desorption measurements, revealing high crystallinity with small crystallite size and large specific surface area.

Keywords Mesoporous TiO$_2$ · Fast sol–gel · Zeta potential · Evolution mechanism

✉ Xiangdong Wang
  wang90xd@163.com

[1] School of Science, Xi'an Jiaotong University, Xi'an 710049, People's Republic of China

[2] School of Textile and Materials, Xi'an Polytechnic University, Xi'an 710048,
  People's Republic of China

✿ Springer

Introduction

Mesoporous TiO$_2$ materials have attracted a lot of research attention due to their commercial availability, unique properties such as large specific surface area, interesting optical and electronic properties, chemical stability, low toxicity, etc. [1–4], highlighting their potential for use in a broad range of technical applications, including dye-sensitized solar cells [5, 6], degradation of pollutants in water and air [7–9], and hydrogen evolution technology [10–12]. However, it is not easy to prepare mesoporous nanoparticles, because the raw materials, synthetic conditions such as the temperature, stirring rate, ionic strength, acidity, and reactant ratios, and the calcination temperature all influence their formation. Although increasing numbers of new methods to prepare mesoporous TiO$_2$ nanoparticles have been introduced, they are all based on hydrothermal synthesis, evaporation-induced self-assembly, precipitation reaction, or the sol–gel process [13–16]. Traditionally, the sol–gel process has been considered to be an attractive method, because it usually proceeds at room temperature and offers various advantages such as high product purity, homogeneous reaction of all the reactants in molecular form, which favors doping, and preparation of mesoporous TiO$_2$ materials with a wide variety of morphologies by adjusting the process conditions [17–20].

Over the last two decades, many studies on mesoporous TiO$_2$ nanostructures produced by the sol–gel method have been reported. Mostly, tetrabutyl titanate, titanium isopropoxide, and titanium tetrachloride are used as precursors, with ionic surfactants (hexadecyltrimethylammonium chloride, ethylammonium nitrate) [21, 22], nonionic surfactants (polyethylene oxide, acetylacetone, polyethylene glycol) [14, 23, 24], block copolymers [P123 (EO$_{20}$PO$_{70}$EO$_{20}$), P127 (EO$_{106}$PO$_{70}$EO$_{106}$), F108 (EO$_{132}$PO$_{50}$EO$_{132}$)], or polydimethylsiloxane (PDMS) [25–28] as template, followed by calcination using different temperatures and gas atmospheres. Yu et al. [29] studied the effects of synthetic conditions such as the temperature, stirring rate, ionic strength, acidity, and reactant ratios on mesoporous materials prepared by the sol–gel method. Robben and coworkers [30] studied the impact of using different gas atmospheres and calcination temperatures on the structural properties of ordered mesoporous TiO$_2$ nanoparticles synthesized via a facile route.

However, to the best of the authors' knowledge, detailed studies of the factors influencing sol–gel formation of mesoporous TiO$_2$ using a bi-template and the effect of calcination temperature on the mesoporous structure have rarely been reported, in particular studies on the process from sol to gel using a dependable and accurate analytical method. However, understanding the effects of factors such as solvent volume, pH, water volume, molecular weights, and the ratio of the two templates on the gel formation as well as the influence of calcination temperature on the crystal size, pore radius, and surface area would be very useful for fabrication of such mesoporous materials.

In the present work, mesoporous TiO$_2$ materials were prepared via a facile and fast sol–gel method combined with two-step calcination at different temperatures under nitrogen and air atmosphere, using tetrabutyl titanate as precursor with polyethylene glycol (PEG) and polyacrylamide (PAM) as bi-template. To track the

fast sol–gel process, we applied analysis based on zeta potential measurements as a more accurate analytical method to investigate the effects of factors such as solvent volume, pH of sol–gel reaction, and PEG molecular weight on the reaction rate of the sol–gel process. The IR spectrum was also used to investigate the reaction mechanism of the fast sol–gel method. The calcined samples were characterized by X-ray diffraction analysis, transmission electron microscopy, and N$_2$ adsorption–desorption measurements.

Materials and methods

Preparation of mesoporous TiO$_2$

All chemicals used in the experiments were of analytical reagent grade and purchased from Shanghai Chemical Reagent Co. Ltd., Shanghai, China. Mesoporous TiO$_2$ was synthesized by a fast sol–gel process. Tetrabutyl titanate (TBOT, 10 mL) was dissolved in 200 mL anhydrous ethanol under magnetic stirring until homogeneous solution was obtained (solution A). Ethanol (20 mL) along with 10 mL water was used for dissolution of a weighed amount of PEG and PAM, and the pH was adjusted to 3 using nitric acid, followed by vigorous stirring for 0.5 h (solution B). Solution B was added dropwise to solution A under vigorous stirring to form transparent, homogeneous solution. The resulting mixture was stirred at room temperature for 1 h until white gel was obtained. The gel was dried at 80 °C for 4 h to obtain xerogel. As-prepared xerogel was crushed to fine powder and further calcined in a controlled atmosphere furnace (BF-760 Nanjing, China) under N$_2$ atmosphere at different temperatures (350, 450, 500, and 600 °C), then calcined in a muffle furnace (KBF1100 Nanjing, China) under air atmosphere at 450 °C. The heating rates for all samples were 2 °C/min from room temperature with 4 h of holding time at the target temperature and cooling rate of 5 °C/min, to achieve mesoporous samples.

Characterization

To study the effects of the investigated factors, viz. solvent volume, amount of water, medium pH, and amount and molecular weight of PEG added, on the sol–gel reaction rate, corresponding sol–gel reaction systems were designed and run to measure their zeta potential values. For some sol–gel reaction systems for which the reaction lasted 5 min, a certain amount of solution was rapidly taken for measurement of zeta potential values by zeta potential analyzer (PHS-3C, Shanghai, China).

The IR spectrum (TENSOR27, Bruker, Germany) was used to study the reaction mechanism of the fast sol–gel process. X-ray diffraction (XRD) patterns of samples were collected in the 2θ range from 20° to 80° using a Bruker D8 Advance X-ray diffractometer (Germany) at room temperature with Cu K$_\alpha$ radiation ($\lambda = 1.5406$ Å), operated at 40 kV and 100 mA. The obtained data were analyzed using JADE software. Structural data were taken from the Inorganic Crystal

Structure Database (ICSD) [anatase (9854), rutile (62679), and brookite (36410)]. The crystallite size was calculated using the Scherrer equation. N_2 adsorption–desorption measurements were performed at $-196\ ^{\circ}C$ using an AUTOSORB-1 apparatus (ASIMP Quantachrome Instruments, USA). During the equilibration time, the sample cell was isolated to minimize the effective dead volume. Measurements were performed in the relative pressure range from 0.03 to 0.99. The samples were degassed at $200\ ^{\circ}C$ for 2 h. The specific area was calculated by the Brunauer–Emmett–Teller (BET) method, and pore size distributions were determined using the Barrett–Joyner–Halenda (BJH) method according to the adsorption–desorption isotherms. Transmission electron microscopy (TEM) and high-resolution transmission electron microscopy (HRTEM) characterization was conducted at 200 kV using a JEOL JEM-2100F (Japan) field-emission instrument. For TEM and HRTEM characterization, the dried sample was thoroughly sonicated for 0.5 h. One drop of this suspension was placed on a 400-mesh carbon-coated copper grid and left to dry in air.

Results and discussion

## Effect of process parameters on the fast sol–gel synthesis

Zeta potential

In colloid science, the zeta potential is a key parameter used to measure the stability and evolution of colloid systems [31]. In the TBOT–C_2H_5OH colloid system, the $Ti(OH)_4$ colloid particles are positively charged in acidic condition [32], which is beneficial for hydrolysis of the precursor, so the zeta potential is positive. The sol system exhibits high zeta potential, whereas the gel system has low potential. The zeta potential therefore gradually decreases over a certain range during the transition from sol to gel in the colloid system. The zeta potential in the colloid system is usually sensitive to factors such as pH, solvent volume, amount of water, molecular weight of polymer, etc. Therefore, the effect of such factors on the kinetic process during the transition from sol to gel can be conveniently studied by monitoring the response of the zeta potential of the system, enabling determination of optimal parameter values for the sol–gel reaction to fabricate mesoporous TiO_2 materials [33].

Effect of pH

pH is considered to be an important parameter influencing sol–gel systems. Adjusting the pH can control the TBOT hydrolysis process, thereby regulating the charge on the sol particles and influencing the zeta potential of the system. As shown in Fig. 1, the zeta potential of all the colloid systems decreased with time, with the size of the drop clearly depending on the pH from 2 to 6. For sample (a) with pH 2, the zeta potential was initially as high as 269.1 mV but reduced strongly to the lowest value of 46.7 mV after 2 h, indicating gel formation in a

Fig. 1 Zeta potential of sol–gel systems with different pH values: 2 (*a*), 3 (*b*), 4 (*c*), 5 (*d*), and 6 (*e*)
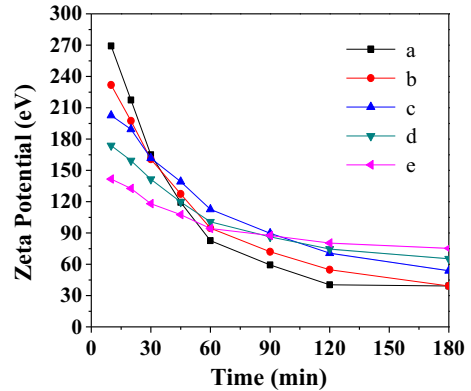
stable system. However, for sample (e) with pH 6 (the highest pH value in this study), the zeta potential changed much less, from a relatively low value of 141.7 mV to reach 87.2 mV after 3 h. Based on these results, it can be concluded that, in the pH range from 2 to 6, the sol–gel reaction rate increased with decreasing pH.

Amount of water used

Similar to the effect of pH, water also plays a key role in the stability of colloid systems. Figure 2 shows the zeta potential for five sol–gel systems containing different amounts of water in the range from 1 to 3 mL in steps of 0.5 mL. This figure shows that, the greater the amount of water added, the higher the original zeta potential, implying a faster sol–gel rate. As shown in Fig. 2a, the zeta potential of the sample with the most water added (3 mL) decreased sharply from 289.1 to 44.8 mV after 2 h, suggesting that it exhibited the fastest gel formation rate. In contrast, as shown in Fig. 2e, the zeta potential of the sample with the least water (1 mL) added showed a weaker decreasing trend from 186.7 to 99.3 mV after 3 h, indicating a slow sol–gel rate with the sample remaining in sol state. The reason is that use of a small amount of water in the sol–gel process results in a slow

Fig. 2 Zeta potential of sol–gel systems with different amounts of water: 3 mL (*a*), 2.5 mL (*b*), 2 mL (*c*), 1.5 mL (*d*), and 1 mL (*e*)
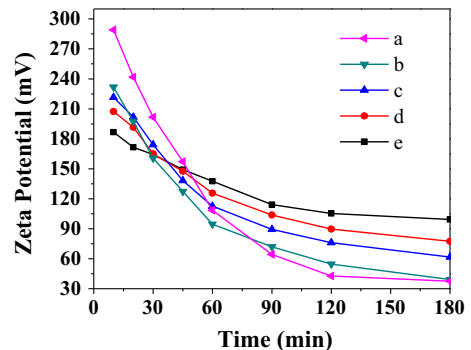
hydrolysis rate of the TBOT precursor so that the hydrolysate reacts with the templates slowly, leading to the observed slow sol–gel rate.

Solvent volume

Figure 3 shows the variation of the zeta potential of systems with different solvent volumes during the sol–gel reaction. The zeta potential of the systems was high and increased with decreasing solvent volume in the system. This effect occurred because decreasing the solvent volume will increase the concentration of sol in the system. The sol particles are therefore closer in the system, resulting in stronger interaction forces between particles and high zeta potential [33]. The zeta potential decreased with time, a trend that was more obvious for systems with smaller solvent volume, as shown in Fig. 3a, b. After 3 h, the zeta potential value of the system with 30 mL of solvent had dropped to 35.7 mV, forming a stable gel. Meanwhile, the potential value for the system with 110 mL of solvent (Fig. 3e) had not changed obviously compared with its initial value, as gel did not form in this system. Based on this analysis, one can adjust the sol–gel process by controlling the volume of solvent. It is concluded that decreasing the solvent volume will increase the sol–gel reaction rate.
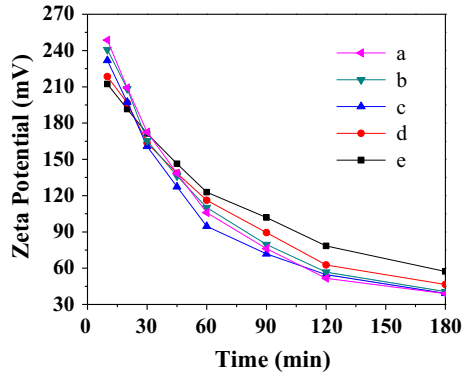
Amount of PEG added

PAM and PEG were used as bi-template in the synthesis of mesoporous TiO_2. The amounts of these templates added can also influence the sol–gel process. In our previous work [34, 35], the influence of PAM on the sol–gel process was already studied. It was found that the amount of PAM added is an important factor influencing the sol–gel process. In the present work, we therefore mainly studied the influence of the amount of PEG added on the sol–gel process. Figure 4 shows the variation of the zeta potential of samples with different amounts of PEG ($M_w = 6000$) added. After 10 min, the potential of all the samples rose to its highest value and sol was fully formed. The potential increased slightly with increasing amount of PEG added. The zeta potential decreased with time but tended

Fig. 3 Zeta potential of sol–gel systems with different solvent volumes: 30 mL (*a*), 50 mL (*b*), 70 mL (*c*), 90 mL (*d*), and 110 mL (*e*)
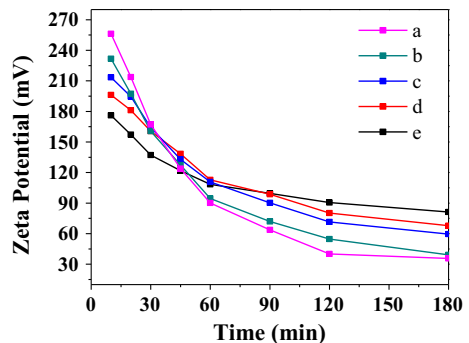
Fig. 4 Zeta potential of sol–gel systems with different amounts of PEG added: 2.5 g (*a*), 2.0 g (*b*), 1.5 g (*c*), 1.0 g (*d*), and 0.5 g (*e*)


to remain stable after 3 h, when gel formed. It is clear from these results that the sol–gel rate was enhanced by increasing the amount of PEG added.

Molecular weight of PEG

There is little research on the effect of template molecular weight on the sol–gel process, but this factor is also significant. In this part of the work, the bi-template comprised PAM with fixed M_w value of 300,000 but PEG with different M_w values. Figure 5 shows the variation of the zeta potential of the samples obtained using PEG with different M_w values from 600 to 20,000. For the samples obtained using PEG with high M_w values of 10,000 and 20,000, the zeta potential was larger and the tendency of its variation was similar, implying that the difference between these two samples did not influence the sol–gel process, in which the template molecules absorb solvent, crosslink, and interact with each other, leading to gel formation. For the samples obtained using PEG with low M_w values of 1000, 2000, and 6000, the trend in the variation of the zeta potential was evidently different. The decrease in the zeta potential was the least for the sample obtained with PEG having M_w of 1000, implying the slowest sol–gel rate. These results show that the rate of the sol–gel reaction decreased with increasing molecular weight of the PEG.

Fig. 5 Zeta potential of sol–gel systems with different molecular weight of PEG: 20,000 (*a*), 10,000 (*b*), 6000 (*c*), 2000 (*d*), and 1000 (*e*)
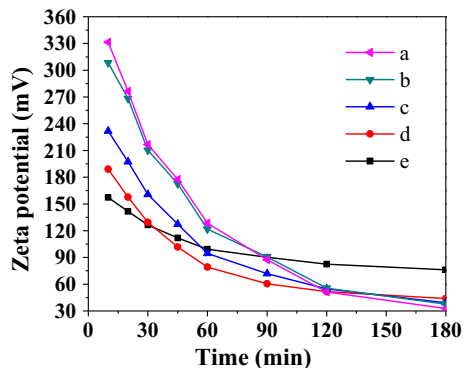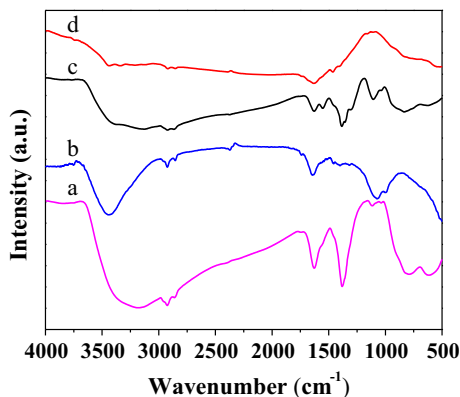
Mechanism of fast sol–gel process

The reaction mechanism of the fast sol–gel process was studied based on the IR spectrum. Figure 6 shows the IR spectra of PEG, PAM, xerogel, and the calcined sample. The peaks observed at 3204.1, 2920.4, 1383.1, 1626.6, and 1121.3 cm^{-1} in Fig. 6a are typical of PEG, whereas the peaks seen in Fig. 6b are characteristic of PAM. The peak at 3419 cm^{-1}, which is weak and wide, corresponds to symmetrical and asymmetric stretching vibrations of O–H and N–H. The peak at 2931.5 cm^{-1} corresponds to C–H stretching vibration. The peaks at 1650.2 and 1156.1 cm^{-1} correspond to C=O symmetrical stretching vibration and –NH_2 flexural vibration, respectively. Compared with Fig. 6a, b, the peaks in Fig. 6c are less sharp, which results from overlap and interlacing of multiplet peaks. The wide peak in the range of 3200–3600 cm^{-1} corresponds to –OH bond in $Ti(OH)_4$ and PEG, –NH bond in PAM, and hydrogen bond interactions of these molecules. The peak at 2900.8 cm^{-1} is caused by C–H bond in PAM and PEG. The peaks at 1554.1 and 1621.2 cm^{-1} correspond to leftward movement of C–O (1626.6 cm^{-1}) in PEG and C=O (1650.2 cm^{-1}) in PAM, further verifying the combination of $Ti(OH)_4$ sol with the templates via hydrogen bonding. In addition, the broad peak at 823.4 cm^{-1} corresponds to Ti–O bond stretching vibration. Compared with the other curves, the peaks in Fig. 6d disappeared, indicating pure TiO_2 with no templates after the calcination process. The weak and wide peak at 3300 cm^{-1} corresponds to –OH bond absorbed on the surface of TiO_2.

Figure 7 presents a schematic that explains the evolution mechanism during the fast sol–gel process. Due to its strong hydrophilicity, PEG can readily combine with titania sol produced by hydrolyzation of tetrabutyl titanate, firstly forming composite grains. These grains then incorporate with PAM to form large composite molecule networks via hydrogen bonding. These hydrogen bonds lead to polymerization crosslinking between hydrolysates of tetrabutyl titanate and templates. This crosslinking is the primary reason for the significantly enhanced sol–gel reaction rate. Finally, mesoporous TiO_2 is obtained by calcination of the xerogel in a two-step process at different temperatures under nitrogen and air atmosphere.

Fig. 6 Infrared spectra of PEG (*a*), PAM (*b*), xerogel (*c*), and calcined sample (*d*)
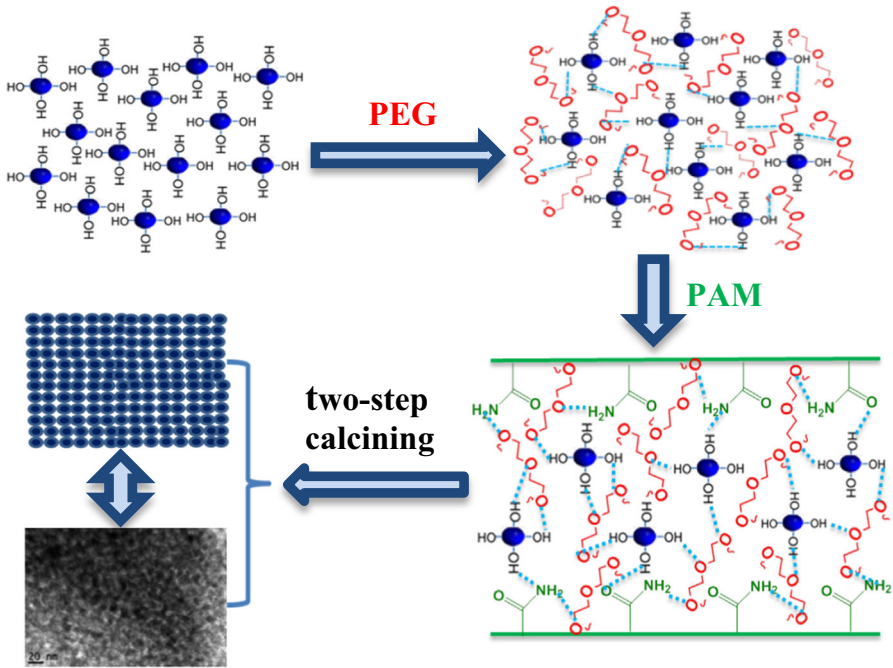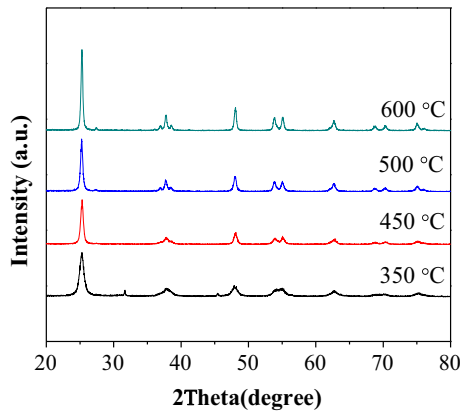
Fig. 7 Evolution mechanism during the fast sol–gel process

Fig. 8 XRD results for samples calcined at different temperatures


Crystal structure and morphology

Figure 8 shows the XRD patterns of TiO$_2$ samples calcined at different temperatures. The crystal phase composition of all samples was anatase TiO$_2$ according to Joint Committee on Powder Diffraction Standards (JCPDS) card no. 21-1272, with no other crystalline impurities detected. The characteristic peaks of mesoporous TiO$_2$ crystals synthesized by the fast sol–gel method were sharp, suggesting high
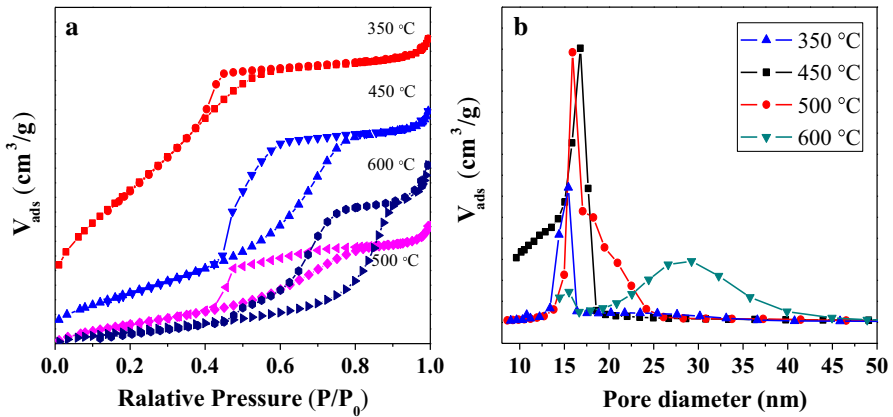
Table 1 Crystallite size of samples obtained using different calcination temperatures	Calcination temperature (°C)	FWHM (°)	Crystallite size (nm)
	350	0.813	10.06
	450	0.427	15.39
	500	0.409	19.88
	600	0.391	23.63

crystallinity, and became sharper with increasing calcination temperature. The average grain size of the samples is presented in Table 1, as calculated using the Scherrer formula from the full-width at half-maximum (FWHM) of the (101) diffraction peak ($2\theta = 25.24°$) of TiO_2, after subtraction of equipment broadening. The small size can be attributed to the bi-template applied in the fast sol–gel method, whose elimination can efficiently decrease the crystal size [36]. The TEM results in Fig. 9a show that the grains were all round shaped with uniform size of about 15.0 nm, consistent with the XRD results. In addition, the samples clearly had typical mesoporous structure with wormhole-like framework. The Debye rings suggest a sequence of diffraction rings consistent with expectations for anatase TiO_2 in a nanocrystalline mesoporous sample. The average interplanar spacing in Fig. 9b was determined to be 0.35 nm, which was assigned to (101) facet of anatase TiO_2 according to the corresponding XRD pattern.

The specific surface area and pore size distribution of the as-prepared mesoporous TiO_2 samples were characterized using nitrogen adsorption–desorption isotherm measurements at 77 K (Fig. 10a). The adsorption–desorption isotherms for all the samples showed typical type IV behavior. Hysteresis loops were observed in the adsorption–desorption isotherms at medium pressure values ($0.4 < P/P_0 < 0.8$), indicating presence of mesoporous structure. For the sample calcined at 600 °C, the hysteresis loop broadened to high pressure ($P/P_0 > 0.8$), indicating mesoporous–macroporous structure at high temperature. To measure the mesopore distribution and surface area of the samples, the BJH and BET methods were applied to the desorption isotherms, respectively. The results are presented in Fig. 10b and Table 2. As expected, the BET surface area (S_{BET}) of mesoporous TiO_2 calcined at
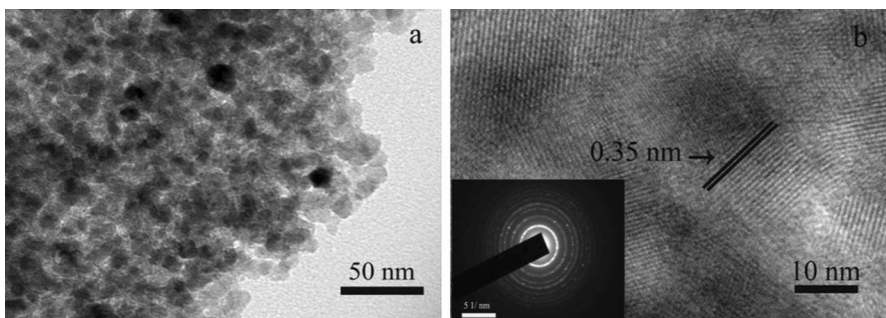
Fig. 9 TEM images of sample

Fig. 10 N$_2$ adsorption–desorption isotherm (a) and pore distribution (b) of samples calcined at different temperatures

Table 2 BET analysis results for samples obtained using different calcination temperatures	Calcination temperature (°C)	S_{BET} (m^2 g^{-1})	V_p (cm^3 g^{-1})	Pore size (nm)
	350	176.35	0.089	15.18
	450	154.37	0.062	16.22
	500	81.44	0.047	18.57
	600	49.97	0.036	28.51

350 °C was as high as 176.35 m^2 g^{-1}, consistent with the adsorption–desorption isotherms and much larger than values for samples synthesized at higher calcination temperatures. This higher S_{BET} value can be attributed to both the increased pore volume (V_p) and decreased pore size resulting from the bi-template applied in the fast sol–gel method [36, 37]. The large S_{BET} and V_p values strongly support the fact that the TiO$_2$ samples had mesoporous structure, formed by agglomeration of and connection between adjacent nanoparticles.

Conclusions

Mesoporous TiO$_2$ samples with high surface area and good crystallinity were synthesized by a fast sol–gel process followed by a two-step calcination process. The fast sol–gel process proceeded well, reducing the reaction time to a few hours, which is attributed to polymerization crosslinking between hydrolysates of Ti alkoxides and the bi-template via intermolecular hydrogen bonding. Factors influencing the kinetic process from sol to gel were investigated by monitoring the zeta potential of different reaction systems. The results showed that lower ethanol volume, lower pH, greater water volume, and higher molecular weight of PEG led to faster sol–gel reaction rate with shorter gelation time. This fast sol–gel

method offers important advantages including low production cost and very fast reaction rate.

References

1. B.C. Qiu, M.Y. Xing, J.L. Zhang, J. Am. Chem. Soc. **136**, 5852–5855 (2014)
2. W. Li, F. Wang, Y.P. Liu, J.X. Wang, J.P. Yang, L.J. Zhang, A.A. Elzatahry, D. Al-Dahyan, Y.Y. Xia, D.Y. Zhao, Nano Lett. **15**, 2186–2193 (2015)
3. W. Li, Z.X. Wu, J. Wang, A.A. Elzatahry, D.Y. Zhao, Chem. Mater. **26**, 287–298 (2014)
4. N.T. Trang, Z. Ali, D.J. Kang, ACS Appl. Mater. Interfaces **7**, 3676–3683 (2015)
5. S. Dadgostar, F. Tajabadi, N. Taghavinia, ACS Appl. Mater. Interfaces **4**, 2964–2968 (2012)
6. T.G. Deepak, G.S. Anjusree, S. Thomas, T.A. Arun, S.V. Nair, A.S. Nair, RSC Adv. **4**, 17615–17638 (2014)
7. H.A. Le, L.T. Linh, S. Chin, J. Jurng, Powder Technol. **225**, 167–175 (2012)
8. E.I. Cedillo-González, R. Riccò, M. Montorsi, M. Montorsi, P. Falcaro, G. Siligardi, Build. Environ. **71**, 7–14 (2014)
9. K.Y. Chen, L.Z. Zhu, K. Yang, J. Environ. Sci. China **32**, 189–195 (2015)
10. A. Najafian, R. Rahimi, S. Zargari, A. Mahjoub-Moghaddas, A. Nazemi, Res. Chem. Intermed. **42**, 3441–3458 (2016)
11. N. Linares, A.M. Silvestre-Albero, E. Serrano, J. Silvestre-Albero, J. García-Martínez, Chem. Soc. Rev. **43**, 7681–7717 (2014)
12. R. Peng, C.K. Lin, J. Baltrusaitis, C.M. Wu, N.M. Dimitrijevic, T. Rajh, S. May, R.T. Koodali, Phys. Chem. Chem. Phys. **16**, 2048–2061 (2014)
13. H. Wang, P.G. Liu, X.S. Cheng, A.Z. Shui, L.K. Zeng, Powder Technol. **188**, 52–54 (2008)
14. I.D. Ivanchikova, M.K. Kovalev, M.S. Mel'gunov, A.N. Shmakov, O.A. Kholdeeva, Catal. Sci. Technol. **4**, 200–207 (2014)
15. R. Miao, Z. Luo, W. Zhong, S.-Y. Chen, T. Jiang, B. Dutta, Y. Nasr, Y.S. Zhang, S.L. Suib, Appl. Catal. B Environ. **189**, 26–38 (2016)
16. W.D. Shi, S.Y. Song, H.J. Zhang, Chem. Soc. Rev. **42**, 5714–5743 (2013)
17. Y. Kuroda, T. Mori, K. Yagi, N. Makihata, Y. Kawahara, M. Nagao, S. Kittaka, Langmuir **21**, 8026–8034 (2005)
18. X.D. Wang, K. Zhang, X.L. Guo, G.D. Shen, J.Y. Xiang, New J. Chem. **38**, 6139–6146 (2014)
19. A. Hernandez-Gordillo, A. Hernandez-Arana, A. Campero, L.I. Vera-Robles, Langmuir **30**, 4084–4093 (2014)
20. N.P. Tangale, P.S. Niphadkar, V. Samuel, S.S. Deshpande, P.N. Joshi, S.V. Awate, Mater. Lett. **171**, 50–54 (2016)
21. S. Biswas, V. Sundstrom, S. De, Mater. Chem. Phys. **147**, 761–771 (2014)
22. J.Y. Shen, H. Wang, Y. Zhou, N.Q. Ye, L.J. Wang, CrystEngComm **14**, 6215–6220 (2012)
23. Y.M. Cui, L. Liu, B. Li, X.F. Zhou, N.P. Xu, J. Phys. Chem. C **114**, 2434–2439 (2010)
24. X. Zhang, V. Thavasi, S.G. Mhaisalkar, S. Ramakrishna, Nanoscale **4**, 1707–1716 (2012)
25. J.M. Du, Z.M. Liu, Z.H. Li, B.X. Han, Y.N. Huang, Y. Gao, Microporous Mesoporous Mater. **83**, 19–24 (2005)
26. G. Marci, E. Garcia-Lopez, M. Bellardita, F. Parisi, C. Colbeau-Justin, S. Sorgues, L.F. Liotta, L. Palmisano, Phys. Chem. Chem. Phys. **15**, 13329–13342 (2013)
27. J.S. Wang, H. Li, H.Y. Li, C. Zou, H. Wang, D.S. Li, ACS Appl. Mater. Interfaces **6**, 1623–1631 (2014)
28. H.G. Wang, P. Chen, X.M. Zheng, J. Mater. Chem. **14**, 1648–1651 (2004)
29. C.Z. Yu, J. Fan, B.Z. Tian, D.Y. Zhao, Chem. Mater. **16**, 889–898 (2004)
30. L. Robben, A.A. Ismail, S.J. Lohmeier, A. Feldhoff, D.W. Bahnemann, J.-C. Buhl, Chem. Mater. **24**, 1268–1275 (2012)
31. D.Q. Lin, L.N. Zhong, S.J. Yao, Biotechnol. Bioeng. **95**, 185–191 (2006)

32. P.O. Vasiliev, B. Faure, J.B. Ng, L. Bergstrom, J. Colloid Interface Sci. **319**, 144–151 (2008)
33. M. Badila, A. Hébraud, C. Brochon, G. Hadziioannou, ACS Appl. Mater. Interfaces **3**, 3602–3610 (2011)
34. J.Y. Xiang, Q.Q. Yin, K. Zhang, X.L. Guo, X.D. Wang, Mater. Technol. **30**, 213–217 (2015)
35. Q.Q. Yin, J.Y. Xiang, X.D. Wang, X.L. Guo, T. Zhang, J. Exp. Nanosci. **14**, 1127–1137 (2016)
36. E.Q. Liu, X.L. Guo, L. Qin, G.D. Shen, X.D. Wang, Chin. J. Catal. **33**, 1665–1671 (2012)
37. K. Zhang, X.D. Wang, T.O. He, X.L. Guo, Y.M. Feng, Powder Technol. **253**, 608–613 (2014)